Nanoscale

PAPER

View Article Online
View Journal



Cite this: DOI: 10.1039/d6nr01383j

# Interface-engineered ZnS QDs@HKUST-1 composite for electrochemical overall water splitting

Ayushi Srivastava, Harsh Dadhania, Kevin Vachhani and Abhishek Dadhania *

The global demand for sustainable hydrogen production continues to accelerate as hydrogen emerges as a cornerstone of the carbon-neutral energy economy. Water splitting provides a clean and scalable pathway for green hydrogen production and sustainable energy development; however, its efficiency is constrained by sluggish reaction kinetics and a lack of catalysts that can simultaneously deliver high activity, stability, and structural tunability, an area that remains scantly explored. Here, we report a ZnS QDs@HKUST-1 (ZQH-1) composite, synthesized *via* a bottle-around-the-ship strategy, as a high-performance bifunctional electrocatalyst for overall water splitting. The synergistic integration of ZnS QDs and HKUST-1 MOF enhances conductivity, strengthens charge interactions, and increases the exposure of metal active sites. Consequently, ZQH-1 achieves low overpotentials of 106 mV for the OER and 140 mV for the HER at 10 mA $cm^{-2}$, alongside excellent durability over 36 h at 10 mA $cm^{-2}$, enabling overall water splitting at only 1.78 V. The physicochemical properties of ZQH-1 were systematically studied using various analytical techniques to investigate its structural features, morphology, chemical composition, and specific surface area. This work demonstrates how interfacial charge dynamics and active-site accessibility govern the catalytic performance of QDs@MOF composites and establishes a general strategy for designing efficient, durable, and low-cost electrocatalysts for sustainable hydrogen production.

Received 8th April 2026,
Accepted 1st June 2026

DOI: 10.1039/d6nr01383j

rsc.li/nanoscale



## 1. Introduction

Hydrogen, the lightest element, carries the heaviest expectations for a carbon-neutral world. With its exceptional energy density, broad applicability across energy sectors, and the ability to produce water as its sole byproduct, hydrogen stands out as the most promising element in shaping the future of sustainable energy systems.[1] Although it can be generated through photocatalysis, natural energy sources, biomass, and electrocatalysis, the large-scale sustainable production of hydrogen remains a significant challenge. Among the various approaches, electrocatalytic water splitting has emerged as the most effective route, due to its efficiency, simplicity, and direct conversion of abundant water into green hydrogen through the hydrogen evolution reaction (HER) and the oxygen evolution reaction (OER).[2] Yet, its efficiency is fundamentally constrained by sluggish reaction kinetics and stability requirements, which drive the applied potential well above the thermodynamic value of 1.23 V *versus* the reversible hydrogen electrode (RHE).[3] Addressing these challenges requires electrocatalysts with abundant active sites and accelerated reaction kinetics that can transform water electrolysis into a practical and sustainable hydrogen-production technology.

Noble metals such as ruthenium dioxide ($RuO_2$) and platinum on carbon (Pt/C) are among the most effective electrocatalysts for water splitting; however, their high cost and limited availability have driven the search for affordable alternatives, including nanostructured transition metals, carbon-based, and metal–organic framework (MOF)-based electrocatalysts.[4–6] MOFs such as ZIF-67,[7] ZIF-8,[8,9] MIL-101,[10] and MOF-74[11] have been extensively explored for electrocatalytic water splitting due to their tunable porous structure, high surface area, and versatile metal–ligand coordination environment, which facilitate charge transfer and catalytic activity. Two-dimensional (2D) MOFs have gained attention as high-performance electrocatalysts, attributable to their intrinsic physicochemical features, including large surface area, porosity, accessible active sites, and enhanced conductivity.[12,13] In recent years, MOFs featuring transition metals such as Ni, Co, Fe, and Mn have been widely studied for water splitting, because of their tunable redox activity and catalytic versatility.[14–16] In particular, 2D Cu-based MOFs have attracted significant attention as promising materials for both HER and OER electrocatalysis. Their high abundance, low toxicity, and rich redox properties make Cu-based catalysts highly favourable for sustainable energy applications. Among them, HKUST-1 (Cu-BTC) stands out due to its high porosity, abundant redox-active sites, open

*Department of Chemical Sciences, P D Patel Institute of Applied Sciences, Charotar University of Science and Technology, Changa - 388421, Gujarat, India.*
*E-mail: abhishekdadhania.bt@charusat.ac.in*

metal centres, and facile synthesis.[17] However, practical applications are limited by poor electrical conductivity and structural instability under electrochemical conditions. These challenges can be effectively addressed by constructing MOF-based composites incorporating nanoparticles, nanorods, nanowires, nanotubes, and quantum dots, where synergistic interaction between MOFs and the incorporated nanostructures enhances stability, conductivity, and overall catalytic performance.[8,18–22]

Quantum dots (QDs), nanoscale semiconductors with sizes typically below 10 nm, offer significant potential as electrocatalytic materials due to their unique quantum-confined electronic properties, high surface area, efficient charge transport, and tunable electronic structures.[23] Several QDs, including metal oxide QDs, graphene QDs, perovskite QDs, carbon QDs, and transition metal sulfide QDs, have attracted significant attention as electrocatalysts due to their high intrinsic activity for both HER and OER.[18,19,24–26] Although transition metal sulfide QDs such as $MoS_2$, $WS_2$, and CdS exhibit rich redox chemistry and tunable electronic structures, their practical applications are constrained by toxicity and structural instability.[16] In contrast, ZnS QDs offer chemical stability, favourable electronic properties, efficient charge transfer and low cost.[27] However, despite their excellent properties, QDs tend to agglomerate, which limits their effectiveness in catalysis, energy conversion, and storage applications. Notably, the high porosity and large specific surface area of MOFs offer an excellent platform for accommodating QDs, preventing their agglomeration, and improving the poor conductivity of pristine MOFs through synergistic integration.[28] Although MOF-based and sulfide-based electrocatalysts have been extensively investigated for water splitting, the interfacial interaction between ZnS QDs and MOF remains comparatively underexplored. Herein, a ZnS QD-engineered HKUST-1 heterostructure was rationally designed to enhance charge transfer, electrical conductivity, and active-site accessibility. The synergistic heterointerface between ZnS QDs and HKUST-1 plays a crucial role in improving the bifunctional electrocatalytic performance toward overall water splitting.

In this study, we present a ZnS QDs@HKUST-1 (ZQH-1) composite designed as a high-performance bifunctional electrocatalyst for overall water splitting. The composite achieves synergistic integration of MOF and QDs by incorporating ultrasmall ZnS QDs into the porous architecture of HKUST-1, where the MOF provides structural stability, high surface area, and abundant accessible active sites, while the QDs contribute tunable electronic properties, quantum confinement effects, and efficient charge transport. The engineered interface in ZQH-1 is expected to enhance charge transfer and increase the accessibility of active sites, thereby giving superior electrocatalytic performance.

# 2. Experimental

## 2.1. Materials

All reagents utilized in this study were of analytical grade and were used without additional purification. Copper(II) acetate monohydrate ($Cu(OAc)_2{\cdot}H_2O$), sodium sulfide nonahydrate ($Na_2S{\cdot}9H_2O$), ethylenediaminetetraacetic acid (EDTA) and benzene-1,3,5-tricarboxylic acid (BTC) were procured from Sigma-Aldrich. *N*,*N*′-Dimethylformamide (DMF) and dichloromethane (DCM) were procured from Aldrich Chemical Pvt. Ltd. Zinc acetate dihydrate ($Zn(OAc)_2{\cdot}2H_2O$) and triethylamine (TEA) were supplied by Sisco Research Laboratories Pvt. Ltd. Distilled water was used in all synthetic procedures.

## 2.2. Preparation of the HKUST-1 MOF

The HKUST-1 was synthesized *via* a solvothermal method using BTC as the organic linker and $Cu(OAc)_2{\cdot}H_2O$ as the metal source.[29] In a typical synthesis, BTC (500 mg, 2.38 mmol) was dissolved in 12 mL of a mixed solvent system comprising DMF, ethanol, and water (1 : 1 : 1, v/v/v). Separately, $Cu(OAc)_2{\cdot}H_2O$ (860 mg, 4.31 mmol) was dissolved in 12 mL of the same solvent system. The two solutions were mixed under continuous stirring, followed by the dropwise addition of triethylamine (0.5 mL). The reaction mixture was continuously stirred at ambient temperature for 24 h. The formed solid product was subsequently isolated by filtration and thoroughly washed twice with DMF.

## 2.3. Preparation of ZnS QDs

The ZnS QDs were synthesized *via* a hydrothermal approach. $Zn(OAc)_2{\cdot}2H_2O$ (0.800 g, 3.64 mmol) was dissolved in 25 mL of deionized water under continuous stirring. Subsequently, EDTA (1.0 g, 3.64 mmol) dissolved in 25 mL of deionized water was added as a capping agent to form a homogeneous solution. In parallel, $Na_2S{\cdot}9H_2O$ (0.285 g, 3.64 mmol) was dissolved in 25 mL of deionized water and subsequently added dropwise to the zinc precursor solution under constant stirring at room temperature. The resulting white suspension was transferred into a Teflon-lined autoclave and heated at 170 °C for 3 h. The precipitated ZnS QDs were collected by centrifugation, thoroughly washed with deionized water, and dried before further use.

## 2.4. Preparation of the ZQH-1 composite

$Cu(OAc)_2{\cdot}H_2O$ (0.344 g, 1.72 mmol) and BTC (0.200 g, 0.95 mmol) were individually dissolved in 12 mL of a DMF/ethanol/water mixture (1 : 1 : 1, v/v/v). Meanwhile, the as-prepared ZnS QDs (0.090 g) were redispersed in 90 mL of the same solvent system and introduced into the copper precursor solution under continuous stirring. Subsequently, the BTC solution was added dropwise to the mixture, which gradually turned blue, and the reaction was then allowed to proceed at room temperature for 24 h. The resulting dark-blue ZQH-1 composite was collected by centrifugation, thoroughly washed with dimethylformamide followed by dichloromethane, and dried overnight at 60 °C for further characterization.

## 2.5. Electrode preparation

For the preparation of the working electrode, 8 mg of synthesized material, 1 mg of carbon black and 1 mg of polyvinylidene fluoride (PVDF) were mixed with 1 mL of *N*-methyl pyrro-

lidone (NMP) to prepare a slurry. A small piece of nickel foam (2 × 1 cm) was first ultrasonicated in 3 M $HNO_3$ solution for 15 min. It was then further washed with water and methanol and kept for drying at 60 °C for 6 h in a hot air oven. The prepared slurry was then directly coated on a nickel foam and dried at 65 °C overnight.

### 2.6. Physicochemical and thermal characterization of the synthesized materials

A powder X-ray diffractometer (PXRD, Bruker, D2 phaser bench-top diffractometer, Cu Kα radiation) was used to confirm the formation of HKUST-1, ZnS QDs and ZQH-1 in the $2\theta$ range of 5° to 70°. Fourier Transform Infrared Spectroscopy (FTIR, Shimadzu) was performed in the range of 400–4000 $cm^{-1}$ to analyse the functional groups and bonding characteristics present in the synthesized materials. The surface morphology of the synthesized materials was examined using transmission electron microscopy (TEM, JEOL JEM-2100) and scanning electron microscopy (SEM, JSM-6010LA). Energy-dispersive X-ray spectroscopy (EDS, Thermo Scientific, Phenom Pharos G2) elemental mapping was performed to confirm the homogeneous distribution of the constituent elements. The thermal stability studies were carried out under nitrogen gas atmosphere using a thermogravimetric analyzer (Mettler-Toledo/DSC-1), and the samples were heated over a temperature range of 30 °C to 800 °C, with a constant heating rate of 5 °C per minute. Inductively coupled plasma optical emission spectroscopy (ICP-OES, Thermo Scientific iCAP 7200 Radial) was conducted to precisely determine the composition of metals in the composite ZQH-1. The elemental composition, chemical bonding and oxidation states of ZQH-1 were determined using X-ray photoelectron spectroscopy (XPS, Thermo Scientific, Nexsa). The structural and vibrational properties of ZQH-1 were analyzed using Raman spectroscopy (Metrohm, Vionic, i-Raman Plus). Brunauer–Emmett–Teller (BET) and Barrett–Joyner–Halenda (BJH) analyses were carried out using a Micromeritics ASAP 2010 instrument to determine the specific surface area and pore size distribution of HKUST-1 and ZQH-1.

### 2.7. Electrochemical measurements

Electrochemical measurements for the OER and HER were carried out on a multichannel electrochemical workstation (Metrohm, Multi Autolab/M 204) using a conventional three-electrode setup. The synthesized materials were used as the working electrode with an exposed area of 1 $cm^2$, a platinum rod served as the counter electrode, and a 3 M KCl-saturated Ag/AgCl electrode was employed as the reference electrode. All experiments were performed at room temperature in 1 M KOH for OER and HER. Cyclic voltammetry (CV), linear sweep voltammetry (LSV) and electrochemical impedance spectroscopy (EIS) were recorded to evaluate the electrocatalytic performance. The non-*iR*-corrected polarization curves are provided in Fig. S9, while all polarization curves were corrected using 95% *iR* compensation. All the measured potentials were converted to the RHE scale for accurate comparison using eqn (1):[30]

$$E_{RHE} = E + 0.059 \times pH + E_{Ag/AgCl} - iR_s \quad (1)$$

where $i$ is the current, $R_s$ is the solution resistance, and $E_{Ag/AgCl}$ is the standard thermodynamic potential for Ag/AgCl, *i.e.*, 0.197. The overpotentials ($\eta$) were calculated using eqn (2) and (3):[19]

$$\eta_{OER} = E_{RHE} - 1.23\ V \quad (2)$$

$$\eta_{HER} = E_{RHE} - 0\ V. \quad (3)$$

The HER proceeds *via* two sequential steps: the initial Volmer step followed by either the Heyrovsky step (electrochemical route) or Tafel step (chemical route). In alkaline electrolytes, water is considered as both the reactant and the proton source for the HER process. In the Volmer step, water molecules are electrochemically reduced, producing hydroxide ions and adsorbed hydrogen intermediates (H*) on the electrode surface. Subsequently, molecular hydrogen is released through either electrochemical desorption (Heyrovsky step) or chemical recombination (Tafel step).[31] The HER kinetics are strongly correlated with the Tafel slope, which provides valuable insight into the underlying reaction mechanism. Under ideal conditions (25 °C and charge-transfer coefficient $\alpha = 0.5$), a Tafel slope of approximately 120 mV $dec^{-1}$ is theoretically expected when the Volmer step is the rate-determining step. This process requires an additional water dissociation step, introducing a higher kinetic barrier, where an electrolyte proton combines with an electron to form adsorbed hydrogen on the electrode surface. Subsequently, $H_2$ formation occurs through one of two pathways: (i) the Heyrovsky mechanism, where adsorbed hydrogen reacts with a proton and an electron to generate $H_2$, or (ii) the Tafel mechanism, where two adjacent adsorbed hydrogen atoms recombine to release $H_2$.[32,33]

In alkaline or neutral conditions, the reaction schemes are: Volmer reaction

$$H_2O + e^- + * \rightarrow H* + OH^- \quad (4)$$

Heyrovsky reaction

$$H* + H_2O + e^- \rightarrow H_2 + OH^- \quad (5)$$

orTafel reaction

$$H* + H* \rightarrow H_2 \quad (6)$$

where * represents the surface-active sites of the catalyst and H* represents the adsorbed hydrogen atoms on the active sites of the catalyst. The rate-determining step is calculated using Tafel slope values. Tafel plots were determined by correlating the overpotential with the logarithm of current density ($\log|J|$). The linear sections of the Tafel plots were fitted using the Tafel equation, and the corresponding Tafel slopes were calculated according to eqn (7):[19]

$$\eta = b \log j + a \quad (7)$$

where the overpotential, Tafel slope, current density, and potential at 10 mA $cm^{-2}$ are represented by $\eta$, $b$, $j$ and $a$, respectively.

The OER is a four-electron-transfer process and has more sluggish reaction kinetics. In both alkaline and neutral electrolytes, hydroxide ions initially adsorb onto the anodic surface, giving rise to surface-bound oxygen species. Subsequent deprotonation of additional hydroxide ions in the presence of these adsorbed intermediates facilitates progressive oxidation steps, ultimately leading to the evolution of molecular oxygen.[34]

The overall process proceeds *via* the adsorbate evolution mechanism (AEM), described by the following elementary steps:

$$OH^- + * \rightarrow HO* + e^- \quad (8)$$

$$HO* + OH^- \rightarrow O* + H_2O + e^- \quad (9)$$

$$O* + OH^- \rightarrow HOO* + e^- \quad (10)$$

$$HOO* + OH^- \rightarrow * + O_2 + H_2O + e^- \quad (11)$$

where * represents the surface-active sites of the catalyst.[26]

## 3. Results and discussion

The ZQH-1 composite was synthesized at room temperature using the bottle-around-the-ship strategy, as shown in Scheme 1. ZnS QDs were synthesized and subsequently incorporated into the HKUST-1 MOF precursor solution, facilitating the growth of the MOF matrix around the QDs to form the ZQH-1 composite. The crystallinity, morphology, composition and thermal stability of the prepared electrocatalyst were characterized by PXRD, TEM, SEM, FTIR, XPS, Raman, EDS, ICP-OES and TGA.

As depicted in Fig. 1(a), the PXRD patterns confirm the crystalline nature and successful formation of ZnS QDs and HKUST-1, and their integration into the ZQH-1 composite, which exhibits distinct diffraction peaks from both components. The PXRD patterns of the synthesized HKUST-1 and ZnS QDs were found to be in good agreement with the reported JCPDS cards 112954 and 05-0566, respectively, with no additional peaks arising from impurities.[35,36] ZnS QDs exhibit characteristic diffraction peaks at 28.63°, 47.74°, and 56.53°, corresponding to the (200), (220), and (311) planes, with calculated *d*-spacings of 0.31 nm, 0.19 nm, and 0.16 nm, respectively. For HKUST-1, the major diffraction peaks appear

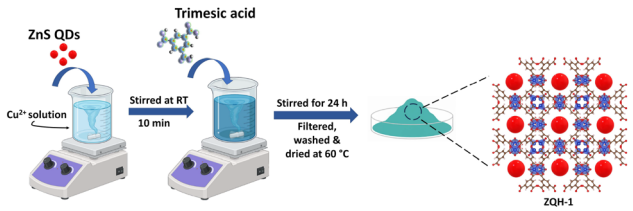


**Scheme 1** Schematic diagram of the synthesis process for ZQH-1.

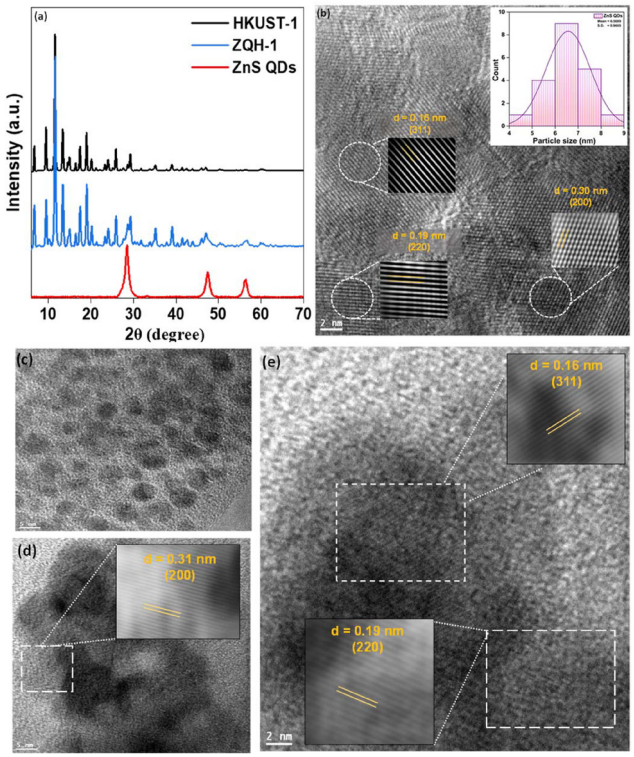


**Fig. 1** (a) PXRD patterns for ZnS QDs, HKUST-1 and ZQH-1 composite. TEM images of (b) ZnS QDs, along with the IFFT images and the inset showing size distribution histogram, (c) HKUST-1, (d) and (e) ZQH-1, along with the IFFT images.

at 6.68°, 9.45°, 11.55°, 13.38°, and 18.99°, indexed to the (200), (220), (222), (400), and (440) planes, with corresponding *d*-spacings of 1.33 nm, 0.93 nm, 0.76 nm, 0.66 nm, and 0.51 nm. The observed *d*-spacings of the ZQH-1 composite closely match with the corresponding HKUST-1 planes (1.31 nm, 0.93 nm, 0.76 nm, 0.66 nm, 0.46 nm) and ZnS QDs planes (0.31 nm, 0.19 nm, 0.16 nm). The ZQH-1 composite exhibits the characteristic reflections of both ZnS QDs and HKUST-1 without significant shifts in diffraction peaks, indicating the structural integrity of the MOF and the incorporation of ZnS QDs. The average crystallite size of the synthesized QDs was estimated using the Debye–Scherrer relation (eqn (12)):[37–39]

$$D = \frac{k\lambda}{\beta \cos\theta} \quad (12)$$

where $\lambda$ represents the X-ray wavelength (here Cu = 0.15414 nm), $\beta$ is the full width at half maximum (FWHM) of the most intense diffraction peak, and $\theta$ is the corresponding Bragg diffraction angle. The calculated mean crystallite size of the ZnS QDs is 7.79 nm, confirming their nanoscale dimensions. The average crystallite size of the ZQH-1 and HKUST-1 was calculated to be ~41 nm and ~42 nm, respectively. The synthesized ZnS QDs (F-43 m) and HKUST-1 (Fm$\bar{3}$m) exhibit a face-centered cubic lattice with unit cell parameters $a = b = c =$ 5.34 Å and $a = b = c =$ 26.34 Å, respectively, consistent with those reported in the literature.[35,36]

In order to reinforce the crystallinity confirmed by PXRD, TEM characterization was conducted, offering a detailed visualization of the microstructure, QD size, and their dispersion within the composite matrix. Fig. 1(b) displays the TEM image of the ZnS QDs, showing their uniform dispersion, near-spherical morphology, and a mean particle size of ~6.6 nm, as indicated by the particle size histogram shown in the inset. The corresponding inverse fast Fourier transform (IFFT) images, shown in Fig. 1(b), reveal distinct lattice fringes for the ZnS QDs with *d*-spacing of 0.31 nm, corresponding to the (200) facet, *d*-spacing 0.19 nm, assigned to the (220) facet, and *d*-spacing of 0.16 nm, corresponding to the (311) facet. These results are consistent with the XRD data, confirming the quantum-scale dimensions and high crystallinity of the ZnS QDs. As MOFs are made up of metal centers and organic linkers, they can be easily damaged under electron beam irradiation during TEM characterization.[13] Consequently, HKUST-1 in Fig. 1(c) exhibits an amorphous appearance. TEM micrographs of the ZQH-1 composite displayed in Fig. 1(d) and (e) clearly show ZnS QDs uniformly integrated within the MOF matrix, with distinct lattice fringes of 0.31 nm, 0.19 nm, and 0.16 nm corresponding to the (200), (220), and (311) planes, confirming their stable incorporation. The observations clearly demonstrate that the crystalline ZnS QDs remain encapsulated within the MOF, while the overall structural integrity of the ZQH-1 composite is well preserved.

The elemental composition and distribution of the ZQH-1 composite were analysed by energy-dispersive X-ray spectroscopy (EDS) coupled with FE-SEM. Elemental mapping (Fig. S1(a)–(f)) reveals the uniform distribution of Zn, S, Cu, C, and O throughout the sample, confirming the homogeneous incorporation of ZnS QDs within the MOF framework. The EDS spectrum (Fig. S1(g)) and corresponding quantitative analysis (Fig. S1(h)) revealed the presence of C (55.33%), O (28.17%), Cu (8.79%), Zn (4.43%), and S (3.28%). The EDS-derived Cu : Zn ratio (~2 : 1) aligns with the expected composition, confirming ZnS QDs encapsulation within the MOF matrix.

Fig. 2(a) presents the FTIR spectra obtained over the range of 4000–400 $cm^{-1}$ to investigate the chemical interactions and bonding environment of the ZnS QDs, Cu metal centers, and organic linkers of HKUST-1. All three synthesized materials exhibited a broad absorption band around 3400 $cm^{-1}$, corresponding to the O–H stretching vibrations of hydroxyl groups from surface-adsorbed water molecules. Also, the band observed in the ZnS QDs and ZQH-1 at 1632 $cm^{-1}$ could be attributed to the H–O–H bending vibration of adsorbed water.[40,41] The absorption peaks in ZQH-1 observed at 630 and 432 $cm^{-1}$ are attributed to the Zn–S stretching vibration mode, red-shifted from those of ZnS QDs (670 and 477 $cm^{-1}$), while the Cu–O stretching vibration of HKUST-1 (484 $cm^{-1}$) exhibits a blueshift to 490 $cm^{-1}$. These shifts indicate strong interfacial interactions, confirming ZnS incorporation, which modifies the Cu coordination environment within the composite. The retention of the benzene-substituted Cu signals, asymmetric ($\nu_{as}$) and symmetric ($\nu_s$) stretching vibrations of carboxylate groups in ZQH-1, indicates structural preservation of the HKUST-1 framework.

TGA was performed to assess the thermal stability, decomposition pathways, and the presence of physically or chemically adsorbed species in HKUST-1, ZnS QDs and ZQH-1. Fig. 2(b) depicts the multi-stage decomposition profiles for all materials, with the inset showing their respective derivative (DTG) curves, conducted over a temperature range of 30 °C to 800 °C under a $N_2$ atmosphere at a heating rate of 5 °C $min^{-1}$. HKUST-1 exhibits a four-step weight loss decomposition. The first decomposition comprised an initial loss of 10% centered at 60 °C due to the desorption of physically adsorbed water. The second decomposition step showed a minor 5% loss at ~210 °C, ascribed to the removal of coordinated water or oxygenated moieties of functional groups. Further, the third decomposition step at 275 °C with 8% weight loss indicates initial decarboxylation and partial breakdown of the BTC linker. Lastly, the fourth decomposition stage had the fastest rate of weight loss from 290 to 370 °C, attributed to decomposition of the organic framework, leaving a residual mass of ~20.5% CuO and $Cu_2O$. In contrast, ZnS QDs display excellent thermal robustness, showing only a small loss near 50 °C from surface water and a negligible ~2% loss at ~600 °C due to volatilization of residual sulfur species, with a total weight loss of only ~12%. The ZQH-1 composite exhibits a distinct three-step decomposition pattern. Firstly, a 10% weight loss at 60 °C, indicating the loss of physically adsorbed water. The incorporation of ZnS QDs shifts and consolidates the second and third thermal events of HKUST-1 into a single peak at 250 °C with 14% weight loss, suggesting that the presence of ZnS QDs changes the decomposition behaviour of the framework. The third and final step involves the degradation of the linker between 290–370 °C, resulting in framework collapse and a higher residual mass (~23%) compared to pristine HKUST-1. This enhanced residue suggests a stabilizing role of ZnS QDs within the MOF matrix. Collectively, these observations confirm that ZnS incorporation not only preserves the intrinsic decomposition profile of HKUST-1 but also imparts improved thermal stability to the composite.

To gain deeper insight into the surface chemistry and interfacial electronic coupling in ZQH-1, XPS measurements were

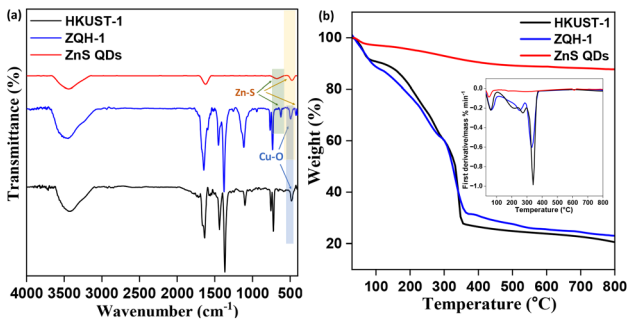


**Fig. 2** (a) FTIR spectra for ZnS QDs, HKUST-1 and ZQH-1 composite and (b) TGA curves for ZQH-1, HKUST-1 and ZnS QDs, with the inset showing the respective DTG curves.

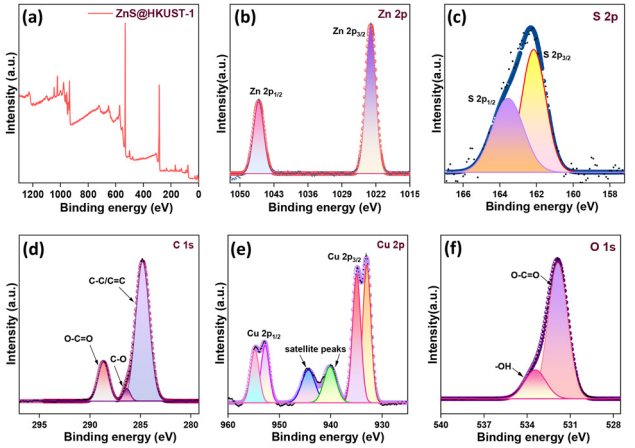


**Fig. 3** (a) XPS full scan spectra and high-resolution XPS spectra for (b) Zn 2p, (c) S 2p, (d) C 1s, (e) Cu 2p and (f) O 1s of the ZQH-1 composite.

performed, as shown in Fig. 3. The XPS survey scan, depicted in Fig. 3(a), confirms the presence of O 1s, Zn 2p, S 2p, C 1s, and Cu 2p elements in ZnS@HKUST-1. Fig. 3(b) depicts the high-resolution Zn 2p spectrum, exhibiting two characteristic peaks at binding energies of about 1020.98 eV and 1042.06 eV, which can be ascribed to Zn $2p_{3/2}$ and Zn $2p_{1/2}$ for $Zn^{2+}$ in the ZnS QDs, respectively. Furthermore, Fig. 3(c) reveals the high-resolution S 2p spectrum, showing two binding energy peaks at 162.9 eV and 164.3 eV, which belong to the S $2p_{3/2}$ and S $2p_{1/2}$ of $S^{2-}$, respectively. The C 1s spectrum depicted in Fig. 3(d) displays three peaks at 284.87 eV (C–C/C=C), 286.2 eV (C–O/C–O–C), and 288.6 eV (O–C=O). Moreover, the Cu 2p spectrum shown in Fig. 3(e) exhibits peaks at 933.1 eV and 953.0 eV corresponding to the Cu $2p_{3/2}$ and Cu $2p_{1/2}$ of $Cu^{2+}$, which are consistent with the $Cu^{2+}$ valence state in HKUST-1 MOF. Additionally, intense shake-up satellite peaks in the 940–945 eV region confirm the +2 oxidation state of copper and exclude the presence of $Cu^0$ or $Cu^+$ species.[42,43] In the O 1s spectrum (Fig. 3(f)), peaks at 531.9 eV and 533.6 eV correspond to carboxylate oxygen (O–C=O) coordinated with $Cu^{2+}$ centers and hydroxyl groups. It is worth noting that the binding energies of Zn 2p and S 2p of the ZnS component in ZQH-1 shifted toward lower energy, while Cu 2p, C 1s, and O 1s all shifted towards higher binding energy, suggesting that electrons might have migrated from the HKUST-1 to the ZnS QDs, thereby increasing the electron density at the ZnS sites. Such redistribution of charge is consistent with interfacial electronic coupling across the ZnS–HKUST-1 heterojunction.[44] Specifically, Zn 2p and S 2p exhibit a negative binding energy shift relative to standard ZnS (1021.0/1044.0 eV for $Zn^{2+}$ and 164.0/165.0 eV for $S^{2-}$), reflecting increased electron density at the ZnS surface, whereas the C–C/C=C and $Cu^{2+}$ peaks exhibit a positive binding energy shift relative to their standard positions (285.1 for C and 931.0/951.0 eV for Cu), signifying reduced electron density on aromatic carbons and $Cu^{2+}$ centers due to electronic coupling with ZnS QDs. These binding energy shifts and preserved oxidation states confirm strong interfacial electronic coupling in ZQH-1, which is expected to enhance charge separation and electrocatalytic performance. The relative atomic concentrations show that the oxygen and carbon concentrations are around 30.6% and 36.1%, which is mainly due to the presence of the organic moiety present in the HKUST-1 framework. Further, copper (20.0%) is more abundant than zinc (10.78%), as expected, while sulfur has a much lower proportion (2.40%) because the ZnS QDs are embedded within the framework or less exposed on the outer surface, whereas Cu sites are more surface-accessible due to their position in the MOF backbone.

In conjunction with XPS, ICP-OES was used to determine the bulk composition of the composite, confirming the expected elemental ratios throughout the composite ZQH-1. The complete elemental composition details are included in Table S1. The results indicated a Cu concentration of 39.743 ppm and a Zn concentration of 20.66 ppm, reflecting the presence of both the HKUST-1 and the ZnS QDs. The Cu : Zn concentration ratio of 2 : 1 (39.7 [≈40] ppm Cu and 20 ppm Zn) aligns well with the intended stoichiometry and supports the successful integration of ZnS within the HKUST-1 matrix. Comparing XPS, EDS and ICP-OES data, the Cu : Zn ratio is ~2 : 1, which is closely aligned, indicating the relatively uniform distribution of the metal species throughout the composite.

The Raman spectra of pristine HKUST-1, ZnS QDs, and ZQH-1 were analysed to gain insight into the interfacial coupling within the composite (Fig. S3). The spectrum of HKUST-1 exhibits the characteristic vibrational features of the BTC linker and Cu units, consistent with the reported spectral features of HKUST-1. The peaks at 738, 819, and 885 $cm^{-1}$ are assigned to the out-of-plane C–H bending vibrations of the aromatic ring, while the peaks at 1006 and 1606 $cm^{-1}$ correspond to the aromatic C=C stretching vibrations. The prominent peaks at 1456 and 1551 $cm^{-1}$ are attributed to the symmetric and asymmetric stretching vibrations of coordinated carboxylate (O–C–O) groups. In the low-wavenumber region, the doublet at 416 and 500 $cm^{-1}$ arises from Cu–O stretching vibrations, whereas the peaks at 167 and 208 $cm^{-1}$ are associated with Cu–Cu stretching modes. The peak at 274 $cm^{-1}$ corresponds to Cu–$O_w$ vibrations, where $O_w$ denotes the oxygen atom of adsorbed water molecules.[45] In addition, the D and G peaks of conductive carbon appear at 1338 and 1586 $cm^{-1}$, respectively. The Raman spectrum of ZnS QDs shows five distinct peaks at 148, 213, 246, 431, and 460 $cm^{-1}$, which are characteristic of nanocrystalline ZnS. The peaks at 148 and 213 $cm^{-1}$ are attributed to the transverse acoustic (TA) and longitudinal acoustic (LA) phonon modes, respectively, due to quantum confinement in the QDs. The peaks at 246 and 431 $cm^{-1}$ correspond to the transverse optical (TO) and longitudinal optical (LO) phonon modes, while the peak at 460 $cm^{-1}$ is attributed to the TO + LA combination mode.[46–48] The Raman spectrum of ZQH-1 retains the characteristic vibrational features of both HKUST-1 and ZnS, confirming the coexistence of both components in the composite. The BTC-related vibrations are observed at 743, 826, and 889 $cm^{-1}$,

while the aromatic C=C stretching peaks appear at 1003 and 1605 $cm^{-1}$. The carboxylate stretching modes remain at 1458 and 1551 $cm^{-1}$, although the asymmetric O–C–O vibration becomes weaker, indicating electronic interaction between ZnS QDs and the coordinated carboxylate groups. Moreover, the Cu–O stretching doublet shifts from 416 and 500 $cm^{-1}$ in pristine HKUST-1 to 402 and 497 $cm^{-1}$ in ZQH-1, accompanied by reduced intensity of the Cu–Cu peaks and a shift of the Cu–$O_w$ vibration from 274 to 269 $cm^{-1}$. These systematic peak shifts and intensity variations indicate that the local coordination environment and electron density around the Cu centers are altered upon coupling with ZnS quantum dots. Such interfacial interactions promote charge redistribution and facilitate electron transport across the heterointerface, thereby enhancing the intrinsic electrocatalytic activity of ZQH-1.

The specific surface area and pore size distribution of HKUST-1 and ZQH-1 were investigated using BET and BJH analysis. Fig. S2 presents the $N_2$ adsorption–desorption isotherms along with the corresponding pore size distributions of both materials. HKUST-1 and ZQH-1 exhibit type-IV isotherms accompanied by pronounced hysteresis loops, confirming the presence of mesoporous architectures. Notably, ZQH-1 displays a significantly enhanced BET surface area of 945.29 $m^2\ g^{-1}$ compared to HKUST-1, which exhibits a surface area of 797.52 $m^2\ g^{-1}$, indicating that the incorporation of ZnS QDs effectively increases the accessible active surface area of the MOF. This enhancement can be attributed to the homogeneous anchoring of ultrasmall ZnS QDs onto the HKUST-1 framework, which inhibits pore collapse while generating additional surface-active sites. Furthermore, although HKUST-1 commonly exhibits a type-I isotherm due to its intrinsic microporosity, the observed type-IV hysteresis loop in both samples can be attributed to the presence of hierarchical porosity and interparticle mesoporosity generated during the MOF and composite formation process.[49,50] The incorporation of ZnS QDs likely modifies the pore architecture and particle packing, resulting in combined micro/mesoporous characteristics rather than indicating framework collapse. Importantly, the retained high surface area together with the characteristic XRD peaks confirms that the HKUST-1 framework integrity is well preserved after composite formation. The BJH pore size distribution reveals mesoporous characteristics for both samples, with average pore diameters of 26.42 Å for HKUST-1 and 21.10 Å for ZQH-1. The decrease in pore size upon incorporation of the ZnS QDs suggests partial pore filling and framework modulation, which contributes to the formation of a more compact yet accessible mesoporous network. Such synergistic structural advantages are expected to play a crucial role in enhancing the electrocatalytic performance of ZQH-1.

## 4. Electrocatalytic performance

The electrochemical properties of ZQH-1 were studied using linear sweep voltammetry (LSV), electrochemical impedance spectroscopy (EIS), cyclic voltammetry (CV) and chronoamperometry measurements in 1 M KOH solution using Ag/AgCl as the reference electrode.

The electrocatalytic HER activity of the synthesized materials was studied in the presence of 1 M KOH electrolyte with a three-electrode system. Fig. 4(a) presents the LSV curves (*iR* corrected) of the synthesized materials obtained at a scan rate of 5 mV $s^{-1}$. Comparing the HKUST-1 MOF, ZnS QDs and ZQH-1 composite, ZQH-1 shows better HER activity. When the current density reaches 10 mA $cm^{-2}$, the overpotential is 140 mV, whereas for the HKUST-1 and ZnS QDs, the overpotentials are 212 mV and 175 mV, respectively. The blank NF electrode exhibited a relatively high HER overpotential of 267 mV at 10 mA $cm^{-2}$, demonstrating substantially lower catalytic activity than the ZQH-1 electrocatalyst. The superior HER performance of ZQH-1 is attributed to the formation of a heterostructure between the ZnS QDs and the HKUST-1 framework, which promotes efficient charge separation, accelerates electron transport, and provides abundant catalytic sites, thereby lowering the overpotential and enhancing overall activity. Tafel analysis was performed to obtain a mechanistic understanding of the HER reaction mechanism, evaluated from LSV using eqn (10). As shown in Fig. 4(b), the Tafel slope of ZQH-1 was found to be 132 mV $dec^{-1}$, which is much smaller than the observed Tafel values for HKUST-1 (220 mV $dec^{-1}$) and ZnS QDs (170 mV $dec^{-1}$). The smaller slope value indicates that ZQH-1 possesses more favourable HER kinetics, requiring less energy to drive the hydrogen evolution reaction at a given current density. Typically, a Tafel slope in this range corresponds to the Volmer–Heyrovsky pathway, in which the electrochemical adsorption step (Volmer reaction) serves as the rate-determining step. The enhanced kinetics of ZQH-1 can be ascribed to the synergistic combination of the high intrinsic activity of ZnS QDs, the porous framework of HKUST-1, and the facilitated charge transfer at the heterojunction interface. Electrochemical impedance spectroscopy (EIS) was performed to determine the charge-transfer resistance. According to the

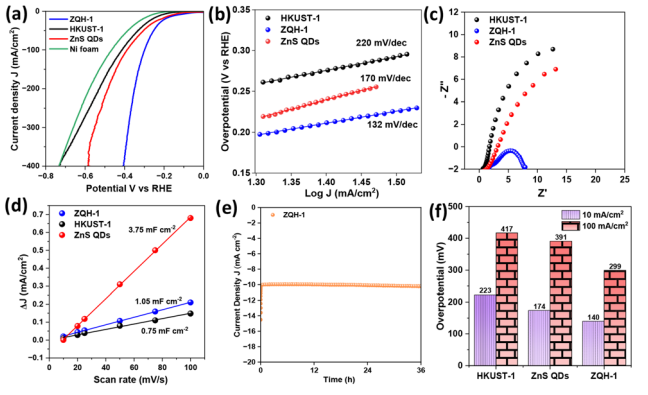


**Fig. 4** HER performances in a 1 M KOH solution. (a) LSV curves at a scan rate of 5 mV $s^{-1}$, (b) Tafel plots obtained from LSV curves, (c) Nyquist plots, (d) $C_{dl}$ plots, (e) chronoamperometry curve of ZQH-1 composite, and (f) overpotential of ZQH-1, HKUST-1 and ZnS QDs@10 and 100 mA $cm^{-2}$.

Nyquist plots (Fig. 4c), ZQH-1 shows the lowest interfacial charge-transfer resistance ($R_{ct}$) value of 6.28 Ω cm$^{-2}$ compared to HKUST-1 (20.29 Ω cm$^{-2}$) and ZnS QDs (16.76 Ω cm$^{-2}$), showing that this electrocatalyst is effective for the HER process with the least resistance to charge transfer and demonstrating accelerated interfacial electron transport. The double-layer capacitance ($C_{dl}$) at the electrode and electrolyte interface, reflecting the electrochemically active surface, was derived from cyclic voltammograms collected at varying scan rates (10–100 mV s$^{-1}$) in 1 M KOH (Fig. S3). The $C_{dl}$ curves were linearly fitted with minimum error, with an $R^2$ value of 99%. The $C_{dl}$ value of ZQH-1 was found to be 1.05 mF cm$^{-2}$, which is higher than that of HKUST-1 (0.75 mF cm$^{-2}$), as depicted in Fig. 4(d). The electrochemical surface area (ECSA) was estimated from the $C_{dl}$ of the electrocatalysts according to eqn (13):[26]

$$\mathrm{ECSA} = \frac{C_{dl}}{C_s}. \quad (13)$$

In this equation, $C_s$ is the specific capacitance of the catalyst, which typically lies in the range of 0.02–0.06 mF cm$^{-2}$ for a flat surface.[26] Based on the conventional reported values, a value of 0.040 mF cm$^{-2}$ was adopted for the ECSA calculations in this study. The ECSA was calculated and was found to be 26.3 cm$^2$ for ZQH-1 as compared to 18.8 cm$^2$ for HKUST-1, reflecting a larger accessible electrochemical surface and higher density of active sites. Despite ZnS QDs exhibiting a larger electrochemically active surface area (ECSA) than ZQH-1, their HER/OER performance was markedly inferior. In contrast, ZQH-1 demonstrated superior electrocatalytic activity, evidenced by lower overpotentials, reduced charge-transfer resistance, and smaller Tafel slopes. These results indicate that the enhanced HER/OER performance of ZQH-1 originates primarily from improved intrinsic catalytic activity arising from the synergistic interfacial interaction between the Cu–MOF framework and ZnS quantum dots, rather than solely from surface area effects. This is consistent with previously reported literature where composites outperform their individual components in catalytic activity despite lower ECSA values.[51] The ZQH-1 composite showed superior long-term electrochemical stability, retaining its performance during extended electrolysis in 1 M KOH. Fig. 4(e) shows the chronoamperometry test, which was accomplished at an overpotential of 140 mV, during which the electrode exhibited no appreciable loss in activity over 36 h while sustaining a current density of 10 mA cm$^{-2}$. As illustrated in Fig. 4(f), the comparative overpotential values at benchmark current densities of 10 and 100 mA cm$^{-2}$ distinctly underline the superior HER performance of ZQH-1 over the pristine materials.

The electrochemical activity of the synthesized material towards the OER was evaluated in 1 M KOH using ZQH-1 as the working electrode. The *iR*-corrected polarization curves (Fig. 5a) clearly demonstrate the superior performance of ZQH-1 compared to pristine HKUST-1 and ZnS QDs. ZQH-1 exhibited a remarkably low overpotential of only 106 mV to achieve a current density of 10 mA cm$^{-2}$, significantly outperforming HKUST-1 (299 mV) and ZnS QDs (118 mV). For the OER, the blank NF electrode required an overpotential of 468 mV to achieve 10 mA cm$^{-2}$, which is markedly higher than that of ZQH-1, highlighting the superior catalytic performance of the composite catalyst. Moreover, at higher current densities, the performance gap becomes more pronounced. ZQH-1 reached 400 mA cm$^{-2}$ at 1.6 V *vs.* RHE, whereas both HKUST-1 and ZnS QDs required ~2.3 V *vs.* RHE to deliver a similar current. Such low overpotential at both low and high current densities highlights the practical applicability of ZQH-1 as a robust OER electrocatalyst. Fig. 5(b) presents the Tafel plots of the synthesized catalysts, revealing a slope of 121 mV dec$^{-1}$ for ZQH-1, which is substantially lower than that of HKUST-1 (298 mV dec$^{-1}$) and ZnS QDs (278 mV dec$^{-1}$). The reduced slope shows the accelerated reaction kinetics and explains the superior electrocatalytic activity of ZQH-1, confirming the favourable charge-transfer dynamics of the composite.

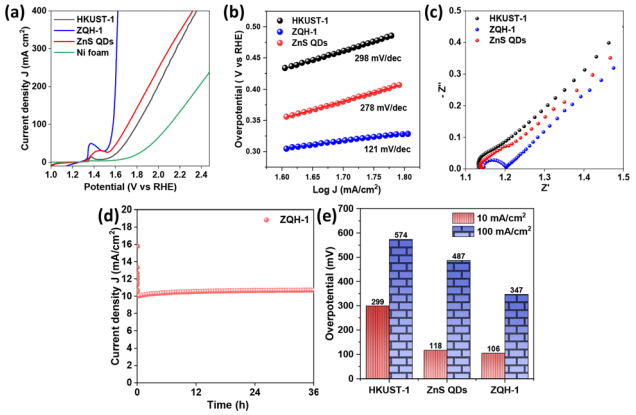


**Fig. 5** OER performances in a 1 M KOH solution. (a) LSV curves at a scan rate of 5 mV s$^{-1}$, (b) Tafel plots obtained from LSV curves, (c) Nyquist plots, (d) chronoamperometry curve of ZQH-1 composite, (e) overpotential of ZQH-1 at 10 and 100 mA cm$^{-2}$.

As electrocatalytic performance is strongly governed by interfacial charge-transfer kinetics, EIS was carried out to evaluate the charge-transfer characteristics of the catalyst. Fig. 5(c) displays the Nyquist plots fitted with an equivalent circuit (Fig. S4) to quantify the charge-transfer resistance, $R_{ct}$, and it can be observed that the ZQH-1 possessed the lowest $R_{ct}$ value of 0.06 Ω cm$^2$, which demonstrates accelerated charge transport across the electrode–electrolyte interface and enhanced OER kinetics, consistent with the above electrochemical results. Given that long-term operational stability is vital for real-world OER applications, Fig. 5(d) shows the ZQH-1 chronoamperometry tested at an overpotential of 106 mV, which retained a current density of ~10 mA cm$^{-2}$ for 36 hours, indicating good operational stability with insignificant performance loss. Fig. 5(e) shows the comparative bar plot of overpotential at 10 mA cm$^{-2}$ and 100 mA cm$^{-2}$ for ZQH-1, HKUST-1 and ZnS QDs, highlighting the superiority of ZQH-1 over the individual components. All these results demonstrate that incorporating ZnS QDs in the HKUST-1 MOF

matrix significantly improves the OER intrinsic activity. This improvement is ascribed to the dual advantages: (i) ZnS QDs decorating the HKUST-1 surface or pore walls, thereby preventing framework collapse and maintaining open porosity, and (ii) enhanced charge transfer and additional active interfaces introduced at the Zn–S and Cu–O coordination junctions.

The synthesized ZQH-1 electrocatalyst exhibits lower HER and OER overpotentials than previously reported Cu–MOF-, ZnS QD- and MOF/QD-based catalysts, while showing competitive performance compared to high-performance non-precious metal and commercial precious metal catalysts (Tables S2 and S3), highlighting its potential as a robust bifunctional catalyst. To validate this, we extended our investigation to overall water splitting in an alkaline medium. Therefore, the electrocatalytic competence of ZQH-1 was assessed in a two-electrode system, with ZQH-1 employed as both the anode and cathode, combining HER and OER activities. As shown in Fig. 6(a), the *iR*-corrected linear sweep voltammetry profile reveals that ZQH-1 requires a low operating voltage of only 1.78 V to achieve the benchmark current density of 10 mA $cm^{-2}$, and further sustains a high current density exceeding 400 mA $cm^{-2}$ at the potential value of 2.45 V. The EIS analysis of the ZQH-1‖ZQH-1 two-electrode system, shown in Fig. 6(b), revealed a low charge-transfer resistance (~0.2–0.3 Ω), indicating rapid interfacial electron-transfer kinetics and efficient charge transport during overall water splitting. The electrode stability was assessed by chronoamperometric testing at 10 mA $cm^{-2}$ in 1.0 M KOH (Fig. 6c). Impressively, ZQH-1 exhibited negligible performance degradation over 36 h of continuous operation under ambient conditions, underscoring its robustness and durability for practical overall water-splitting applications. Following the long-term stability test, the post-electrolysis LSV curves of the ZQH-1‖ZQH-1 system, depicted in Fig. S8, exhibit minor deviation from the initial polarization profiles, indicating excellent electrochemical durability and sustained catalytic activity during prolonged overall water-splitting operation. To further investigate the structural robustness of the catalysts after electrolysis, comprehensive post-characterization analyses were performed using Raman spectroscopy, PXRD, XPS, and SEM. As shown in Fig. S3(b), the post-stability Raman spectrum of pristine HKUST-1 exhibits two additional peaks at 485 and 688 $cm^{-1}$, which are attributed to Cu–O vibrational modes associated with $CuO/Cu_2O$ species generated through partial hydrolysis and oxidation of the Cu paddlewheel units during electrolysis. In contrast, these features are absent in the post-stability spectrum of ZQH-1, indicating that the incorporation of ZnS QDs effectively stabilizes the Cu coordination environment and suppresses extensive framework degradation. This observation suggests that the ZnS/HKUST-1 heterointerface promotes controlled surface reconstruction while preserving the structural integrity of the composite. The structural stability of the catalysts was further examined by PXRD analysis before and after the durability test (Fig. S7). The diffraction patterns remain largely unchanged after electrolysis, with the dominant reflections at $2\theta \approx 44.5°$ and 51.8° corresponding to the Ni foam substrate. Notably, ZQH-1 exhibits nearly identical pre- and post-stability diffraction patterns without the appearance of additional impurity peaks, demonstrating the excellent crystalline stability of the heterostructure under alkaline operating conditions. Post-electrochemical measurements, XPS analysis of ZQH-1 (Fig. S4) confirms the retention of Zn, S, Cu, C, and O species after prolonged catalytic operation. The Zn 2p peaks at 1021.6 and 1044.0 eV indicate the persistence of $Zn^{2+}$ species associated with ZnS QDs, whereas the weakened S 2p intensity suggests partial surface sulfur depletion and electrochemical surface reconstruction during the OER. Additionally, the enhanced O–C═O contribution in the C 1s spectrum together with the O 1s features associated with metal–oxygen/hydroxyl species indicate the formation of oxygen-containing surface species under anodic conditions. These results collectively suggest that ZQH-1 undergoes partial surface reconstruction into catalytically active oxygenated species while maintaining the essential ZnS–HKUST-1 heterostructure. Furthermore, SEM images recorded after the stability test, shown in Fig. S10, reveal that ZQH-1 largely preserves its porous and uniformly distributed surface morphology with only minor surface roughening, whereas pristine HKUST-1 exhibits noticeable aggregation and partial structural degradation after electrolysis. The preserved morphology of ZQH-1 further confirms the strong interfacial interaction between the ZnS QDs and the HKUST-1 framework, which effectively suppresses structural collapse during extended operation.

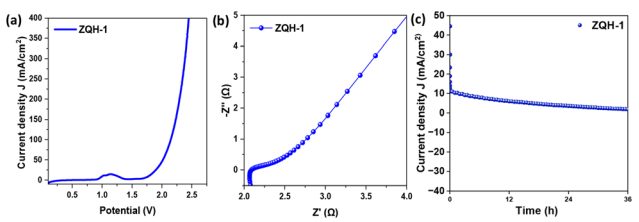


**Fig. 6** (a) LSV curve at a scan rate of 5 mV $s^{-1}$ with ZQH-1 as both cathode and anode, (b) Nyquist plot, and (c) chronoamperometry curve for 36 h.

## 5. Conclusions

In summary, this work reports the successful development of ZQH-1 as a highly efficient bifunctional electrocatalyst for overall water splitting. The ZQH-1 composite demonstrates remarkable bifunctional electrocatalytic activity toward water splitting, arising from the synergistic combination of the highly porous framework and redox-active sites of HKUST-1 with the accelerated charge-transfer dynamics introduced by ZnS QDs. Benefiting from these merits, ZQH-1 exhibited excellent bifunctional electrocatalytic activity in 1.0 M KOH, delivering low overpotentials of 106 mV for the OER and 140 mV for the HER at a current density of 10 mA $cm^{-2}$, while maintaining impressive operational stability over 36 h at 10 mA $cm^{-2}$. In addition, its lower Tafel slope and $R_{ct}$ values confirm accelerated charge-transfer kinetics at the electrode–electrolyte inter-

face. Moreover, ZQH-1 showed outstanding electrocatalytic activity, producing a current density of 10 mA $cm^{-2}$ at 1.80 V for overall water splitting. The excellent electrocatalytic properties of ZQH-1 can be ascribed to its optimized composition and strong electronic interactions between the ZnS QDs and the HKUST-1 framework, which collectively expose abundant active sites and facilitate efficient charge transport. The facile synthesis, high activity, and long-term stability position ZQH-1 as a promising non-noble-metal electrocatalyst for sustainable hydrogen production. This work broadens the library of advanced TMS QD-based electrocatalysts and provides new insights for the rational design of high-performance catalysts toward overall water splitting.

## Author contributions

Ayushi Srivastava: methodology, data curation, investigation, formal analysis. Harsh Dadhania and Kevin Vachhani: investigation and formal analysis. Abhishek Dadhania: conceptualization, supervision, writing – review & editing.

## Conflicts of interest

There are no conflicts to declare.

## Data availability

The data supporting this article have been included as part of the supplementary information (SI). Supplementary information is available. See DOI: https://doi.org/10.1039/d6nr01383j.

## Acknowledgements

The authors gratefully acknowledge Charotar University of Science and Technology (CHARUSAT) for providing the necessary research facilities. Financial support received from Education Department, GoG under SHODH (ScHeme of Developing High Quality Research) scheme and CHARUSAT PhD Scholar's Fellowship (CPSF) (A. S. and H. D.), CSIR-JRF (File No. 09/1294(18332)/2024-EMR-I) (K. V.) is gratefully acknowledged.

## References

1 S. Aslam, S. Rani, K. Lal, M. Fatima, T. Hardwick, B. Shirinfar and N. Ahmed, *Green Chem.*, 2023, **25**, 9543–9573.
2 Y. Jiao, Y. Zheng, M. Jaroniec and S. Z. Qiao, *Chem. Soc. Rev.*, 2015, **44**, 2060–2086.
3 A. Zhou, D. Song, Z. Hui, J. Yang, W. An, X. Zuo, X. Ye and M. Jiang, *Results Phys.*, 2024, **59**, 107611.
4 S. Mukhopadhyay, O. Basu, R. Nasani and S. K. Das, *Chem. Commun.*, 2020, **56**, 11735–11748.
5 M. Nemiwal, V. Gosu, T. C. Zhang and D. Kumar, *Int. J. Hydrogen Energy*, 2021, **46**, 10216–10238.
6 W. Wang, X. Xu, W. Zhou and Z. Shao, *Adv. Sci.*, 2017, **4**, 1600371.
7 H. S. Jadhav, H. A. Bandal, S. Ramakrishna and H. Kim, *Adv. Mater.*, 2022, **34**, 1–74.
8 Y. Pan, K. Sun, S. Liu, X. Cao, K. Wu, W. C. Cheong, Z. Chen, Y. Wang, Y. Li, Y. Liu, D. Wang, Q. Peng, C. Chen and Y. Li, *J. Am. Chem. Soc.*, 2018, **140**, 2610–2618.
9 S. V. P. Vattikuti, K. C. Devarayapalli, N. K. R. Nallabala, T. N. Nguyen, N. N. Dang and J. Shim, *J. Phys. Chem. Lett.*, 2021, **12**, 5909–5918.
10 X. G. Peng, X. D. Li, L. P. Cui, Z. H. Gao, W. Huang and Z. J. Zuo, *Ranliao Huaxue Xuebao*, 2021, **49**, 1354–1361.
11 W. Zhou, Z. Xue, Q. Liu, Y. Li, J. Hu and G. Li, *ChemSusChem*, 2020, **13**, 5647–5653.
12 Y.-H. Zhu, S.-L. Shi, Z.-T. Bo, B.-Z. Zhang, W.-M. Xiao, S.-H. Wang and C. Chen, *Small*, 2025, **21**, 2501812.
13 Q. Hong, Y. Wang, R. Wang, Z. Chen, H. Yang, K. Yu, Y. Liu, H. Huang, Z. Kang and P. W. Menezes, *Small*, 2023, **19**, 1–9.
14 L. Wei, X. Zhang, Z. Xu, X. Shu, H. Lou, F. Lan, S. Gu, G. Chen, Q. Zeng, M. Sui and X. Ke, *J. Energy Chem.*, 2026, **116**, 854–862.
15 W. Wu, Z. Gao, Q. Li, Z. Wang, S. Liu, H. Wu, Y. Zhao, Y. Jiao and X. Zhao, *J. Energy Chem.*, 2022, **74**, 404–411.
16 Y. Guo, T. Park, J. W. Yi, J. Henzie, J. Kim, Z. Wang, B. Jiang, Y. Bando, Y. Sugahara, J. Tang and Y. Yamauchi, *Adv. Mater.*, 2019, **31**, 1807134.
17 B. Ren, Q. Yi, F. Yang, Y. Cheng, H. Yu, P. Han, Y. Yang, G. Chen, I. Jeerapan, Z. Li and J. Z. Ou, *Energy Fuels*, 2022, **36**, 8381–8390.
18 X.-B. Meng, J. L. Sheng, H. L. Tang, X. J. Sun, H. Dong and F. M. Zhang, *Appl. Catal., B*, 2019, **244**, 340–346.
19 J. Lin, H. Zhou, R. S. Amin, A. E. Fetohi, K. M. El-Khatib, C. Wang, L. Guo and Y. Wang, *Inorg. Chem. Front.*, 2023, **10**, 1294–1304.
20 B. Chen, G. Ma, Y. Zhu and Y. Xia, *Sci. Rep.*, 2017, **7**, 1–9.
21 Z. Zhao, J. Hao, B. Jia, X. Zhang, G. Wu, C. Zhang, L. Li, S. Gao, Y. Ma, Y. Li and P. Lu, *J. Energy Chem.*, 2023, **83**, 79–89.
22 W. Huang, C. Peng, J. Tang, F. Diao, M. N. Yesibolati, H. Sun, C. Engelbrekt, J. Zhang, X. Xiao and K. S. Mølhave, *J. Energy Chem.*, 2021, **65**, 78–88.
23 K. Agarwal, H. Rai and S. Mondal, *Mater. Res. Express*, 2023, **10**, 062001.
24 K. Kumari and M. Ahmaruzzaman, *Mater. Res. Bull.*, 2023, **168**, 112446.
25 D. Pan, L. Wang, Z. Li, B. Geng, C. Zhang, J. Zhan, L. Yin and L. Wang, *New J. Chem.*, 2018, **42**, 5083–5089.
26 H. S. Gugtapeh and M. Rezaei, *ACS Appl. Nano Mater.*, 2024, **7**, 2086–2099.
27 G. Asghar, M. Fiaz, M. A. Farid, M. N. Ashiq and M. Athar, *Int. J. Hydrogen Energy*, 2024, **51**, 1435–1447.

 

28 L. Giri, S. R. Rout, R. S. Varma, M. Otyepka, K. Jayaramulu and R. Dandela, *Nanotechnol. Rev.*, 2022, **11**, 1947–1976.
29 D. J. Tranchemontagne, J. R. Hunt and O. M. Yaghi, *Tetrahedron*, 2008, **64**, 8553–8557.
30 A. T. A. Ahmed, A. S. Ansari, S. M. Pawar, B. Shong, H. Kim and H. Im, *Appl. Surf. Sci.*, 2021, **539**, 148229.
31 A. Raveendran and R. Dhanusuraman, *RSC Adv.*, 2023, **13**, 3843–3876.
32 B. S. Reghunath, S. Rajasekaran, K. R. S. Devi, D. Pinheiro and U. C. J. R. Jaleel, *Int. J. Hydrogen Energy*, 2023, **48**, 2906–2919.
33 M. R. Subramaniam, S. Ramakrishnan, S. Sidra, S. C. Karthikeyan, S. Vijayapradeep, J. Huang, M. Mamlouk, D. H. Kim and D. J. Yoo, *J. Mater. Chem. A*, 2024, **12**, 5967–5979.
34 K. K. Joshi, S. V. Chauhan, P. M. Pataniya and C. K. Sumesh, *Int. J. Hydrogen Energy*, 2024, **58**, 1562–1575.
35 S. S. Y. Chui, S. M. F. Lo, J. P. H. Charmant, A. G. Orpen and I. D. Williams, *Science*, 1999, **283**, 1148.
36 A. Asif, M. S. Sreevidya, K. Archana and N. G. Pillai, in *Materials Today: Proceedings*, Elsevier Ltd, 2020, vol. 41, pp. 665–668.
37 B. M. Raffah, H. Hassan, M. W. Iqbal and Y. Al-Hadeethi, *Energy Fuels*, 2024, **38**, 3477–3490.
38 D. S. Sharma, A. P. Patel, S. N. Bariya, Y. G. Kapdi, S. S. Soni, N. N. Patel, S. H. Panjabi and V. K. Patel, *ACS Appl. Electron. Mater.*, 2024, **6**, 3617–3629.
39 A. P. Patel, D. S. Sharma, S. N. Bariya, Y. G. Kapdi, J. D. Solanki, S. S. Soni, V. K. Patel and S. H. Panjabi, *J. Mater. Chem. A*, 2024, **13**, 680–695.
40 P. Sakthivel, S. Muthukumaran and M. Ashokkumar, *J. Mater. Sci.: Mater. Electron.*, 2015, **26**, 1533–1542.
41 A. B. Alwany, G. M. Youssef, E. E. Saleh, O. M. Samir, M. A. Algradee and A. Alnehia, *Optik*, 2022, **260**, 169124.
42 M. Chen, R. Abazari, S. Sanati, J. Chen, M. Sun, C. Bai, A. M. Kirillov, Y. Zhou and G. Hu, *Carbon Energy*, 2023, **5**, e459.
43 T. Van Tran, D. T. C. Nguyen, T. T. Nguyen, H. T. N. Le, C. Van Nguyen and T. D. Nguyen, *J. Water Process Eng.*, 2020, **36**, 101319.
44 J. Chen, S. Lv, Z. Shen, P. Tian, J. Chen and Y. Li, *ACS Sustainable Chem. Eng.*, 2019, **7**, 13805–13814.
45 M. Todaro, A. Alessi, L. Sciortino, S. Agnello, M. Cannas, F. M. Gelardi and G. Buscarino, *J. Spectrosc.*, 2016, **2016**, 8074297.
46 S. Elsi, S. Mohanapriya and K. Pushpanathan, *J. Supercond. Novel Magn.*, 2020, **33**, 3223–3240.
47 A. Kaderavkova, L. Loghina, M. Chylii, S. Slang, P. Placek, B. Frumarova and M. Vlcek, *J. Alloys Compd.*, 2020, **831**, 154814.
48 E. K. Goharshadi, R. Mehrkhah and P. Nancarrow, *Mater. Sci. Semicond. Process.*, 2013, **16**, 356–362.
49 S. Rouf, Y. E. Greish, B. Van der Bruggen and S. Al-Zuhair, *Carbon Resour. Convers.*, 2024, **7**, 100199.
50 A. Yañez-Aulestia, V. M. Trejos, J. M. Esparza-Schulz, I. A. Ibarra and E. Sánchez-González, *ACS Appl. Mater. Interfaces*, 2024, **16**, 65581–65591.
51 Y. Xue, Y. Guo, Q. Zhang, Z. Xie and J. Wei, *Nano-Micro Lett.*, 2022, **14**, 1–12.